6th European Conference on Computational Mechanics (ECCM 6)
7th European Conference on Computational Fluid Dynamics (ECFD 7)
11-15 June 2018, Glasgow, UK

NUMERICAL INVESTIGATION OF RECTANGULAR FLAT PLATE SLAMMING

Jose D. Mesa, Kevin J. Maki

Department of Naval Architecture and Marine Engineering, University of Michigan
Ann Arbor, Michigan, USA
jmesa@umich.edu, kjmaki@umich.edu

Key words: Plate Ditching, Fluid-Structure Interaction, Slamming Three-Dimensional Effects, Peak Pressure Curvature

Abstract. In this paper, we present the hydroelastic assessment of high-speed flat plate slamming events. The complex water entry problem involves the interaction of the structure with a dense fluid and time-dependent wetness. While the majority of the studies of this problem have been focused on the pure vertical motion, in this study, we primarily focus on the effects of large forward speed on the hydroelastic response of the plate.

The fluid-structure interaction (FSI) methodology used in this work is based on a tightly coupled approach between computational fluid dynamics (CFD) and finite element method (FEM). For the fluid domain, CFD with the volume-of-fluid (VoF) method is applied to solve the air-water interface. For the structure simulation, the commercial software Abaqus is used to discretize the structure with linear dynamic finite elements, and modal decomposition is applied to the FEM model to decoupled and truncated the structural system.

The study examines the hydrodynamic performance and global response of two flat-plate structural arrangements and investigates the importance of three-dimensional flow effects. Rigid body and two-way coupled simulations are presented to investigate and assess the hydroelastic effects of hydrodynamic loading during slamming events.

1 Introduction

The analysis of water entry problems is complex since they involve high localized pressure, complex free surface topology and fluid-structure interaction. In this work, we focus on three interdependent aspects of this slamming problem: the importance of three-dimensional effects on the jet root evolution, the time-dependent wetness that is part of the slamming event, and lastly, the deformation of the structure due to the hydrodynamic loading.

The numerical results for one of the structural arrangements are compared to a theoretical two-dimensional self-similar solution developed by [1]. This theoretical solution is based on a potential flow approach of an ideal incompressible fluid, assuming constant vertical and horizontal velocities during the impact case. The numerical results are further validated using experimental data presented in [2]. The experimental campaign was conducted on CNR-INSEAN for aircraft ditching applications, but the velocity ratio and impact conditions are also suitable for high-speed marine vessels.

2 Numerical Method

The numerical method is based on a coupling between computational fluid dynamics (CFD) and finite element method (FEM). The algorithm allows for either loosely or tightly coupled simulations, depending on the user application. The FSI solver is based on the work presented in [3]. The FSI method is capable of coupling OpenFOAM for the fluid domain and Nastran, Abaqus or an in-house developed FEA solver for the structural domain.

The fluid domain solution is determined using CFD with the volume of fluid approach (VoF). VoF allows for the tracking of the complex non-linear free surface accurately for complex geometries. VoF is used with the Navier-Stokes equations to combine the properties of fluids (air and water) into a single continuous fluid using the volume fraction variable α, as shown in equations 1 through 5.

$$\nabla \cdot \vec{u} = 0 \tag{1}$$

$$\frac{\partial \rho \vec{u}}{\partial t} + \nabla \cdot \rho \vec{u}\vec{u} = -\nabla \bar{p} + \nabla \cdot \left[\mu \left(\nabla \vec{u} + \nabla \vec{u}^T\right)\right] - \rho \vec{g} \tag{2}$$

Where $\vec{u}$ is the fluid velocity, ρ is the fluid density, μ fluid viscosity, $\bar{p}$ fluid pressure and $\vec{g}$ gravitational acceleration.

$$\rho(\vec{x}, t) = \rho_{\text{water}} \alpha(\vec{x}, t) + \rho_{\text{air}}(1 - \alpha(\vec{x}, t)) \tag{3}$$

$$\mu(\vec{x}, t) = \mu_{\text{water}} \alpha(\vec{x}, t) + \mu_{\text{air}}(1 - \alpha(\vec{x}, t)) \tag{4}$$

$$\frac{\partial \alpha}{\partial t} + \nabla \cdot (\alpha \vec{u}) + \nabla \cdot (\alpha(1 - \alpha)\vec{u_r}) = 0 \tag{5}$$

The structural domain is solved using the modal decomposition method within the finite-element approach. The structure is simulated using the commercial software Abaqus. The modal decomposition allows for modal truncation, reducing the complexity of the structure. This selection of modes is based on their energy participation factor in the response. Furthermore, due to the orthogonality of the mode shapes, the system can be

truncated and simplified to a decoupled system of structural equations of motion shown in Equation 6.

$$[I]\{\ddot{q}\} + [2\xi\omega_n]\{\dot{q}\} + [\omega_n^2]\{q\} = \{f\} \tag{6}$$

Both the structural and fluid domains are solved sequentially in an iterative manner by the tightly-coupled solver. The rigid-body fluid stress is averaged at the structural Gauss points; then the velocity is provided at the fluid grid points from the structure-shape functions. Due to the FSI segregated nature, an inertial under-relaxation factor γ introduced in [4] is applied to ensure the stability of the method.

3 Test Case and Numerical Setup

The experimental condition simulated in this study is an aluminum alloy AL2024-T3 plate, 1 m long, 0.5 m wide and 15 mm thick. The outer perimeter of the plate was clamped to a thicker frame on the edges, reducing the elastic impact area to 0.850 m by 0.350 m. The impact setup is pitch angle θ= 10°, vertical velocity V=10 m/s and horizontal velocity U=40 m/s. The test case is labeled condition 1132 in [2]. Velocities in numerical simulation are held constant during the impact. This constraint follows the theoretical solution from [1] and provides an opportunity to more clearly highlight the three-dimensional effects during the slamming event.

The fluid domain discretization is shown in Figure 1. The domain spatial discretization is constant in a region that extends from the leading edge of the plate up to the end of the domain. This region allows for more accurate resolution of the free-surface. A grid refinement study is conducted for the coarse, medium, and fine grids. A summary of the grid resolutions is shown in Table 1.

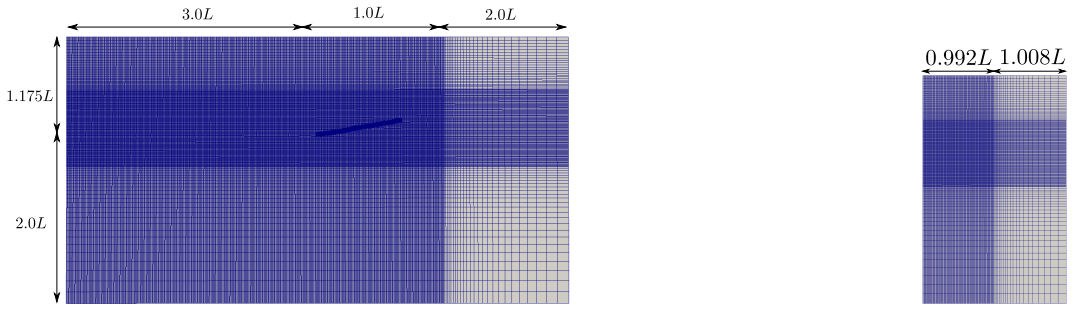

(a) Profile view of CFD mesh

(b) Body plan view of CFD mesh

Figure 1: Fluid domain discritization for coarse grid ($L = 1$ m and $\Delta x = 4$ mm).

The structural domain is discretized using Abaqus SR4 shell elements. Figure 2 displays the final spatial discretization used for the hydroelastic plate response. To ensure

Table 1: CFD grid resolution

	Grid Cells	Plate Faces	Resolution
Coarse	3,091,567	32,629	4 mm
Medium	5,990,979	57,084	3 mm
Fine	15,496,386	128,651	2 mm

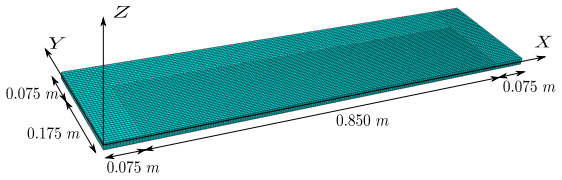

Figure 2: Abaqus structure mesh with symmetry boundary condition on the negative Y direction. Mesh resolution of 5280 SR4 shell elements.

structural domain convergence, two approaches were employed: a modal element frequency convergence and a mode participation factor determined based on modal energy response. Modal element convergence is shown in Figure 3. It can be observed that the first ten modes converge after the FEM mesh reaches 5,280 shell elements. This mesh resolution is selected for the hydroelastic simulations and modal energy response analysis.

The modal energy response of the plate slamming is determined by the modal force generated from a rigid-plate impact. The rigid modal force is obtained in the one-way coupled simulation for the first 25 plate modes. These forces are combined with the transfer function of a damped single degree-of-freedom system to determine the mode participation energy. The first ten modes are sufficient to capture 99.9933% of the total system energy.

4 Rigid-Plate Slamming

The numerical FSI method is used to study the water entry problem of a flat plate with high horizontal speed. Validation and convergence of the fluid domain are performed for the quantities of force components acting on the plate, transverse water surface elevation, local pressure and jet root propagation velocity. Figure 4 shows a comparison of the x and z force components acting on the plate for numerical simulations and experiments. As illustrated in Figure 4 numerical grid convergence on force components acting on the plate is achieved. Excellent agreement between experimental and numerical

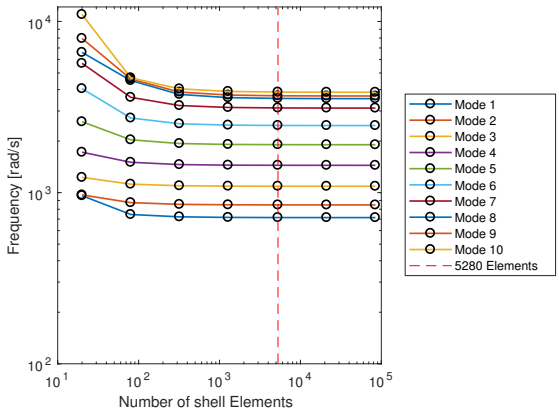

Figure 3: Finite element mesh modal convergence study.

slope and magnitude for the z component of the force is observed. The magnitude and slope of the x component of force is in agreement for all numerical grids and experimental data up to t=0.0042 s. Experimental x force data displays a rapid force fluctuation from t=0.0042-0.0408 s, whereas the numerical simulations maintain a constant negative force during this period. After this period, the experimental force maintains almost a constant negative value until the jet leaves the plate, where a positive slope on the force can be observed. All numerical simulations exhibit a similar trend. The time difference between the change in slope for numerical and experimental results is due to the constant impact velocity constraint that is implemented for the numerical simulations. The absolute jet root propagation velocity is maintained in the simulations, whereas the experiments observed a small velocity reduction during the impact time of approximately 2 m/s.

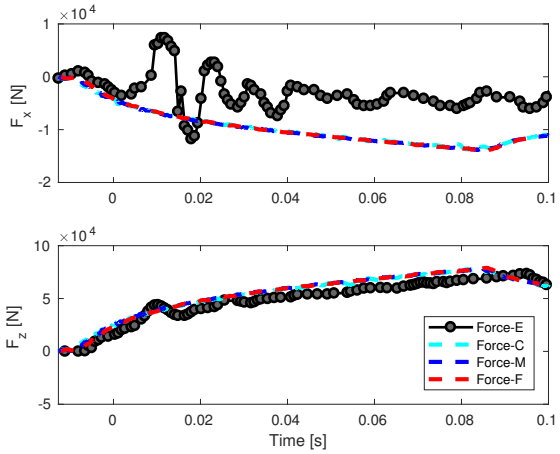

Figure 4: Time history of force components in x (top) and z (bottom) for coarse (C), medium (M), fine (F) grids and experiment (E) for condition 1132.

Figure 5 displays the local pressure time history comparison between the experimental pressure probes and the coarse, medium and fine grids. The reference time used in Figure 5 corresponds to the time where the peak pressure rise occurs at 0.125 m. Excellent agreement between experimental and numerical pressure coefficient is observed. The time difference between numerical values and experimental observations is due to the deceleration of the plate during the impact phase. The numerical method underpredicts the maximum peak pressure observed near the trailing edge of the plate. The experimental value for the pressure coefficient observed at 0.125 m is 1.8, whereas the fine grid estimated a value of 1.43. This underprediction is due to insufficient grid resolution for the pressure integration near the trailing edge. Further grid refinement is necessary for solving high local pressure in this region. Experimental pressure probes exhibit a significant reduction in maximum peak pressure between probes located at 0.125 and 0.400 m and an almost constant peak pressure for following locations. A similar pattern is observed in numerical pressure time history.

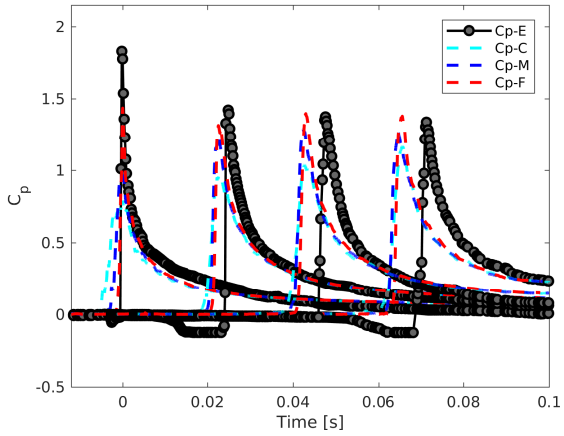

Figure 5: Time history of pressure coefficient c_p recorded at 0.125, 0.400, 0.600 and 0.800 m along the centerline of the plate from the trailing edge for coarse (C), medium (M), fine (F) and experiment (C_p-E) for condition 1132.

Figure 6 shows good agreement between numerical and experimental results on the pressure distribution along plate centerline at the time when the peak arrives at 0.800 m from the trailing edge. Numerical and experimental observations agree on the pressure ratio values with the theoretical solution near the trailing edge of the plate. The pressure ratio values diverge from the theoretical solution as the peak pressure moves along the plate, highlighting the role of possible three-dimensional effects.

Lastly, a transverse water surface elevation comparison among the numerical grids is performed. Figure 7 displays transverse view of the water surface elevation η, located at the plate trailing edge for the full model plate on the right and half model plate on the

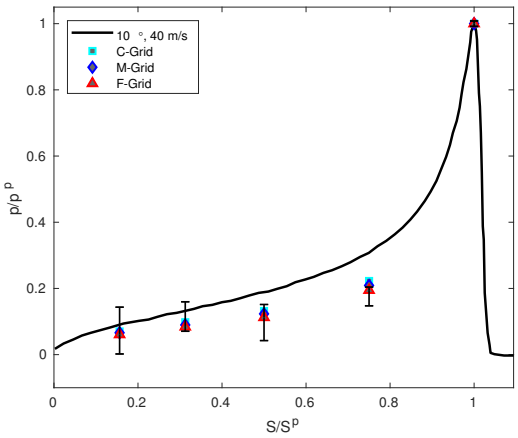

Figure 6: Pressures of probes along the plate centerline at the instant of peak pressure located at 0.800 m from the trailing edge. The horizontal and vertical axes are scaled by the location and pressure of corresponding probe. The solid black line shows the theoretical solution. Error bars represent the experimental dispersion during the test repeats.

left. The horizontal axis is the dimensionless transverse coordinate defined as $\xi = y/B$. Close agreement is observed for the free surface between the medium and fine grids for both the full and half plate models.

5 Jet Root Curvature

Rigid tests with different plate widths are performed to analyze three-dimensional effects. The two plate geometries considered for the three-dimensional effect investigation are 0.5 m and 0.25 m plate widths. The pressure field acting on the plate for six instances in time are analyzed, corresponding to maximum peak pressure arriving at 0.125, 0.250, 0.400, 0.600 and 0.800 m from the trailing edge and when the peak pressure arrives to the leading edge. The maximum peak pressure is extracted and interpolated onto a finer mesh resolution for analysis. A parabolic equation is fit using the least-squares method on the data points to obtain the equation coefficients. The formulation of the problem follows a similar analysis performed by [5], but instead of using the wetted length of the plate the maximum peak pressure location is used. L_i denotes the distance from the trailing edge of the to the geometric intersection between the undisturbed waterplane and the plate. L_p is the x coordinated of where the line of the peak pressure intersects the outer edge of the plate and $d(y)$ defines the curvature of the maximum peak pressure.

The maximum peak pressure location is defined by:

$$x_{\mathrm{p}}(y) = L_{\mathrm{p}} + d(y) \tag{7}$$

$$d(y) = a_0 + a_2 y^2 \tag{8}$$

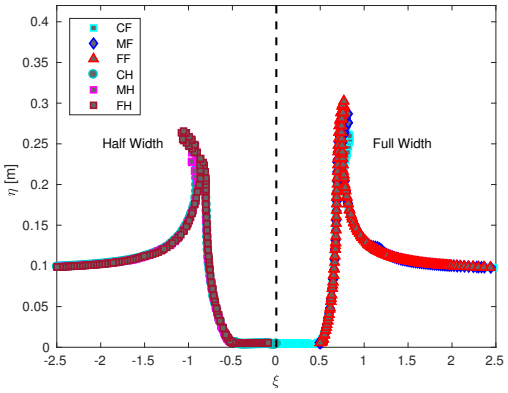

Figure 7: Transverse water surface elevation view at the time when peak pressure arrives at 0.800 m. Full-plate model grids are denoted as CF, MF, and FF for the corse, medium, and fine grids. Half-plate model is denotated as CH, MH, and FH for the coarse, medium and fine respectively.

$$\lambda_i = \frac{L_i}{B} \tag{9}$$

$$\lambda_p = \frac{L_p}{B} \tag{10}$$

$$\xi = \frac{y}{B} \tag{11}$$

$$\delta = \frac{d(y)}{B} \tag{12}$$

Substituting the dimensionless variables defined on equations 9-12, we can express the equation for the curvature of the peak pressure as:

$$\delta(\xi) = \alpha_0 + \alpha_2 \xi^2 \tag{13}$$

Where the dimensionless equation coefficients are defined as:

$$\alpha_0 = \frac{a_0}{B} \tag{14}$$

$$\alpha_2 = a_2 B \tag{15}$$

Figures 8 and 9 display the results of the least-squares method for the unsteady impact condition. The calculated average dimensionless coefficient α_0 and α_2 for all analyzed instances are 0.070 and -0.244 respectively. Figure 10 displays a comparison between the unsteady plate slamming peak pressure location and the steady plate jet root propagation experiments performed by [5]. Figure 10 shows how both the full and half-width plates maximum peak pressure is in agreement with the experimental jet root defined by a curve with the form of $1.60\lambda_i - 0.30\lambda_i^2$ derived in [5].

Figure 11 shows the time delay of the peak pressure, where excellent agreement is observed until halfway along the plate. A significant difference in propagation velocity

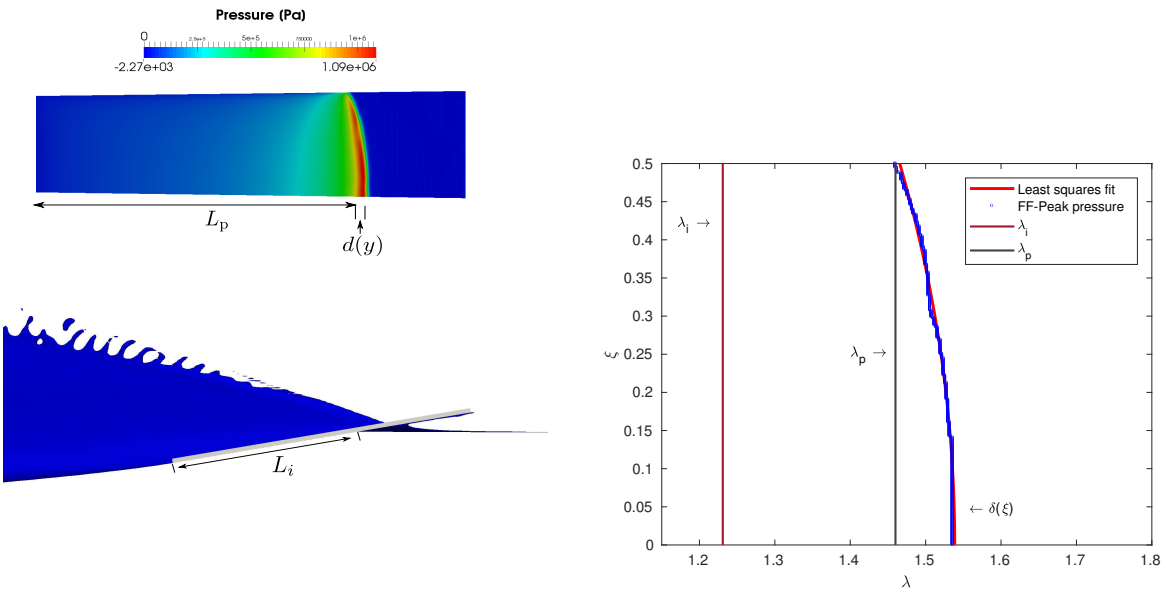

(a) (b)

Figure 8: (a) shows the fine grid pressure field (top) and unsteady geometric intersection between free-surface and plate (bottom) for 0.5 m plate width at t=0.075s and (b) shows the fine grid maximum peak pressure extraction for 0.5 m plate width is denotated by FF-Peak pressure at the same instance in time. The vertical and horizontal axes are dimensionalized by the plate width. λ_i is defined from the trailing edge of the plate until the geometric intersection and λ_p is measured from the trailing edge up to the maximum peak pressure edge point. $\delta(\xi)$ defines the maximum peak pressure curvature from λ_p.

for 0.600 and 0.800 m locations is observed for both numerical and experimental values. As previously explained these differences are due to the absolute plate velocity reduction during the impact phase for experimental repeats. A linear trend in the propagation velocity and a higher value than that of the geometric intersection is observed for all grids and experimental data. The half plate propagation velocity is closer to the predicted theoretical solution. The large pitch angle for the model condition and the reduction in plate width allows for more water to escape from the sides of the plate increasing the three-dimensional effects. These results confirm the role of three-dimensional effects on reducing the jet root propagation velocity and the peak pressure intensity.

6 Hydroelastic Slamming

The hydroelastic validation is performed for the quantity of strain in the axial plate direction. Figure 12 shows the experimental and numerical strain comparison for four discrete points located at the centerline and port edge of the plate. The overall hydroelastic response is captured by the tightly-coupled FSI method. The centerline strain gages S2 and S5 predict higher deformation compared to edge gages S3 and S6 for both numerical

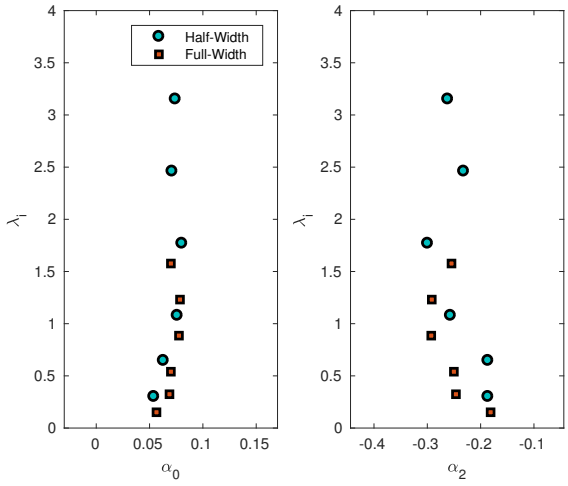

Figure 9: Analytical peak pressure curvature analysis for the two flat-plate structural arrangments. The vertical axis represents the dimensionless geometric intersection for the unsteady motion. The horizontal axes are the dimensionless coefficients as defined in Equations 14 and 15 respectively.

and experimental results. Underprediction and high frequency of oscillation in numerical solution are due to a fully clamped edge boundary condition (BC) assumption. The experimental set-up can be more accurately modeled using a condition between pinned and clamped. Further investigation needs to be performed in this regard since strain is highly sensitive to BC modifications.

7 Conclusions

In this paper, we describe a hydroelastic numerical method used to simulate a flat-plate slamming event. The method is based on a tightly coupled approach between the fluid and structure domains and applicable for high forward-vertical speed ratios, large added mass, and time-dependent wetness problems. The structure is modeled by a linear dynamic solver within the commercial software Abaqus with the modal decomposition method. The fluid domain solution is governed by the Navier-Stokes equations and solved using computational fluid dynamics within OpenFOAM with the volume-of-fluid method.

The CFD method validation is performed for the quantities of local pressure, vertical and longitudinal force components, peak pressure propagation velocity. The tightly coupled method is validated for strain in the axial plate direction. Comparisons are made with the theoretical and experimental results presented in [1]. Also, a comparison is performed for the peak-pressure and jet root curvature presented in [5].

The numerical results show excellent agreement with the experimental data for the force components, local peak pressure, and peak pressure propagation velocity. The numerical strains captured the overall hydroelastic response and tend to slightly underpredict the

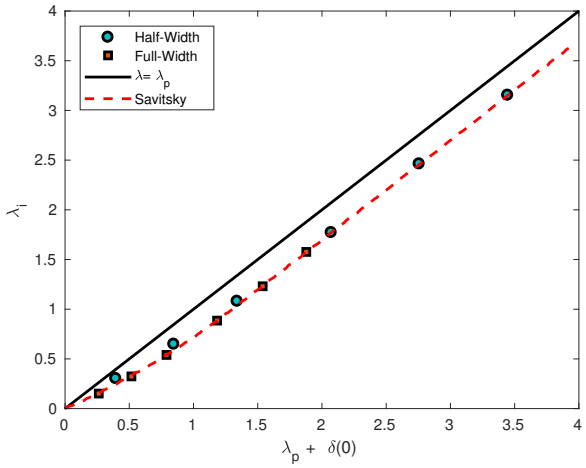

Figure 10: Analytical peak pressure curvature analysis for the two flat-plate structural arrangments.

experimental value. This reduction is due to the fully-clamped edge boundary condition apply to the structure. It is expected that the physical boundary conditions are between a pinned and clamped condition.

Finally, a detailed analysis of the unsteady maximum peak pressure curvature is performed and compared with [5] steady wave rise curvature. Results agree with [5] water rise curvature for both full and half plate widths maximum peak pressure curvature. Three-dimensional effects are highlighted by reducing the jet root propagation speed and increasing the time required for the jet root to fully developed.

REFERENCES

[1] A. Iafrati. Experimental investigation of the water entry of a rectangular plate at high horizontal velocity. *Journal of Fluid Mechanics*, 799:637–672, 2016.

[2] A. Iafrati, S. Grizzi, M. Siemann, and L. B. Montañés. High-speed ditching of a flat plate: Experimental data and uncertainty assessment. *Journal of Fluids and Structures*, 55:501–525, 2015.

[3] D. J. Piro. *A Hydroelastic Method for the Analysis of Global Ship Response Due to Slamming Events*. PhD thesis, The University of Michigan, 2013.

[4] D. J. Piro and K. J. Maki. Hydroelastic analysis of bodies that enter and exit water. *Journal of Fluids and Structures*, 37:134–150, 2013.

[5] D. Savitsky and J. W. Neidinger. Wetted area and center of pressure of planing surfaces at very low speed coefficients. Technical report, Stevens Inst of Tech Hoboken NJ, 1954.

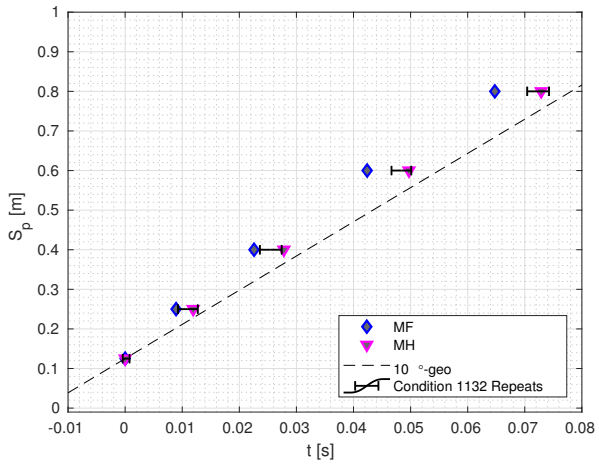

Figure 11: Time delays of centerline pressure probes. The probe location relative to the plate trailing edge is represented by S_p.

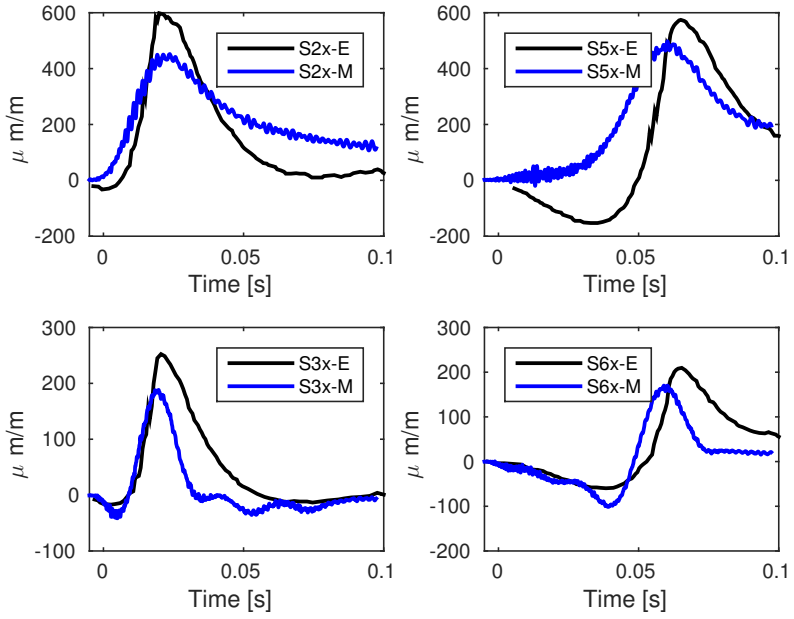

Figure 12: Time history of the strain in x direction for condition 1132